

The role of high-pressure coolant in the wear characteristics of WC-Co tools during the cutting of Ti-6Al-4V

Pietro Stolff^{1*}, Jose Mario Paiva^{1,2}, Yassmin Seid Ahmed^{1,3}, Jose Luis Endrino⁴, Saurav Goel⁴ and Stephen Clarence Veldhuis¹

¹McMaster Manufacturing Research Institute (MMRI), Department of Mechanical Engineering, McMaster University, 1280 Main Street West, Hamilton, ON L8S4L7, Canada; stolff@mcmaster.ca; paivajj@mcmaster.ca; Seidahmy@mcmaster.ca; veldhu@mcmaster.ca

²Mechanical Engineering Graduate Program – PPGEM, Pontificia Universidade Católica do Paraná, Curitiba – 80215901, Brazil

³Production Engineering Department, Alexandria University, Alexandria, 21544, Egypt

⁴School of Aerospace, Transport and Manufacturing, Cranfield University, College Rd, Bedfordshire MK43 0AL, UK; j.l.endrino@cranfield.ac.uk; saurav.goel@cranfield.ac.uk

*Correspondence: stolff@mcmaster.ca; Tel.: +1-905-818-0031

Abstract

Aeronautic applications have been making use of titanium alloys for decades. Ti-6Al-4V is one of the most commonly applied alloys, and although its mechanical properties warrant its acceptance for many applications, the machinability of this alloy remains a challenge. So far, the most successful technique in facilitating this alloy's machining has been the application of High-Pressure Coolant Supply (HPC) on account of its influence on the tribological aspects of the cutting operation. On that premise, this work employs experimental and computational resources to advance the current understanding of the wear mechanism in terms of the tool-chip contact conditions and establish a correlation between coolant pressure, cutting speed, tool life, cutting forces, and chip formation when machining Ti-6Al-4V with HPC supply. Results showed that HPC plays a role in the reduction of tool-chip temperature profiles and contact stresses, positively impacting tool flank wear, oxidation levels and chip formation, also improving chip breakability.

Keywords:

Tool wear, Titanium, High-Pressure Coolant, tribology, FEA, chip formation.

1. Introduction

Ti-6Al-4V is the titanium alloy with the broadest range of applications, accounting for 45-65% of the world's titanium consumption [1]. It is widely applied in the aerospace industry, mainly due to its exceptional specific strength and unmatched mechanical properties [2].

Due to its low thermal conductivity and high chemical reactivity, Ti-6Al-4V is classified as a difficult-to-cut material [3,4]. Titanium machining leads to significantly increased temperatures at the tool/chip interface, even at lower cutting speeds [5]. Furthermore, the Ti and Al (it is made of) present a strong affinity to most tool materials [6], imposing an even bigger challenge to the processing of this alloy. In order to mitigate such effects, a common approach would be the reduction of cutting speed, which directly reduces temperatures in the cutting zone [7]. This would however, adversely affect the production, as low material removal rate (MRR) would increase the demand-supply gaps, making products containing Ti alloys less viable.

Previous researchers have generally made use of coated cutting tools to interfere with the severe interactions taking place during the titanium machining process [8,9]. However, results were not satisfactory when machining Ti and its alloys, as most available coatings are composed of Ti and Al, which would react with the workpiece material. An alternative to the use of tool coatings is the application of cutting fluids to reduce thermal and mechanical loads, especially when working at higher cutting speeds, where heat becomes the main cause for accelerated tool wear [3]. However, conventional coolant supplies do not ensure targeted fluid delivery in the cutting zone and thus, coolant application by traditional means does not achieve significant efficiency [10]. Through careful setup, cutting fluids can be directed towards the primary, secondary, and tertiary shear deformation zones. The secondary shear deformation zone, located at the tool/chip interface, presents a combination of high shear and normal stresses, parallel to the long tool/workpiece contact surface [7]. It consists of the most heat intensive region during the cutting process, requiring substantial cooling action. On that premise, flood coolant supplies can not adequately access the secondary shear deformation zone, due to the barrier imposed by the severe tool/chip contact conditions, resulting in intensive heat generation. To address this issue, different cooling strategies have been employed to improve machining performance of titanium alloys. Cryogenic cooling was deemed a suitable alternative to conventional flood coolant supply when working with low thermal conductivity alloys [11,12]. Conversely, the use of cryogenic cooling significantly increases workpiece material hardness, negatively impacting mechanical

113
114
115 loads and promoting accelerated tool wear rates in the case of Ti alloys [10]. This added to its high
116 operational costs and impact on dimensional control, makes cryogenic machining unfit for these
117 industrial applications. Experiments are reported on the use of Minimum Quantity Lubrication
118 (MQL) for the machining of titanium alloys. The application of MQL was also not proven effective
119 [11–14], since its cooling capabilities are limited when dealing with the high levels of heat imposed
120 by the cutting process.
121
122
123
124

125 A newer alternative emerging in this direction is the use of High-Pressure Coolant (HPC),
126 which is capable of providing a relatively low cost alternative that is able to address most of the
127 aforementioned issues [10,15]. Moreover, the added benefit of using HPC for the machining of Ti
128 alloys is an improved sub-surface integrity [10]. Figure 1 illustrates some of the key benefits
129 provided by the application of HPC to the rake face of the cutting tool. That includes the reduction
130 in chip curl radius, promotion of chip breakability, and heat dissipation from the tool-chip interface
131 [7]. The shorter TCCL (Tool-Chip Contact Length) contributes to lower diffusion wear rates and
132 consequently prolongs the lifespan of the cutting tool [7].
133
134
135
136
137
138

139 As the issue being investigated in this paper i.e. HPC assisted cutting of Ti6Al4V is topical
140 and is in infancy stages of research, many aspects such as chip formation, tool-chip contact
141 conditions and thermal phenomena when machining titanium are hitherto unexplored. Therefore,
142 this work aims to develop a better understanding of the of the wear mechanism, the chip formation,
143 contact conditions and mechanical/thermal aspects of the titanium machining process when
144 employing high pressure coolant supplies at different pressures, combined with multiple sets of
145 cutting parameters. Adding to the experimental findings, computational resources were utilised to
146 study the temperature and stress profiles. The analysis of the collected data allowed for establishing
147 a correlation between: coolant pressure, cutting speed, tool life, cutting forces, wear mechanisms
148 and chip formation.
149
150
151
152
153
154
155
156
157
158
159
160
161
162
163
164
165
166
167
168

2. Materials and methods

2.1 Finite Element Analysis

The finite element analysis (FEA) is an essential tool for the evaluation of cutting conditions, such as temperature/stress profiles within the cutting zone. The primary difficulty in the FEA of metal cutting is capturing the severe plastic deformation of the metal, which results in extreme tribological conditions at the tool-workpiece interface [16].

Modeling of metal machining for turning requires a fundamental understanding of the deformation conditions in the relevant deformation zones, strain rates, as well as the frictional conditions at the tool-workpiece interface. The cutting temperature/stress profile is critical for understanding and controlling the machining process [17].

The numerical analyses present in this work were carried out on a commercial FEA code (Thirdwave's Advantedge CAE software). Advantage employs a Lagrangian approach combined with adaptive remeshing capabilities [18]. This formulation is responsible for addressing the non-linearities caused by the high levels of plastic deformation, strain rates and inherent resolution issues arising during the turning process.

The constitutive model derived from the Cuitino and Ortiz stress update method is employed for the flow stress calculations (eq. 1), where α refers to the strain hardening, $\theta(T)$ to the thermal softening and $\Gamma(\dot{\alpha})$ α $\dot{\alpha}$ T refer to rate sensitivity, equivalent plastic strain, plastic strain rate, and temperature, respectively [19].

$$\sigma(\alpha, \dot{\alpha}, T) = g(\alpha) \theta(T) \Gamma(\dot{\alpha}) \quad (1)$$

Furthermore, the power law (eq. 2) is used to describe strain hardening and rate sensitivity, where reference values for strain and strain rates are denoted by α_0 and $\dot{\alpha}_0$, respectively.

$$g(\alpha) = \left(\sigma_0 \left(1 + \frac{\alpha}{\alpha_0} \right)^{\frac{1}{N}} \right), \Gamma(\dot{\alpha}) = \left(1 + \frac{\dot{\alpha}}{\dot{\alpha}_0} \right)^{\frac{1}{M}} \quad (2)$$

A fifth order polynomial function is used to determine thermal softening (eq. 3) [19].

225
226
227
$$\theta(T) = c_0 + c_1T + \dots + c_5T^5$$
 (3)
228
229

230 Adaptive remeshing capabilities enable the model to account for the element deformations
231 that are intrinsic to the Lagrangian method. Deformations were being constantly monitored,
232 anytime a certain tolerance is met, refinement/coarsening algorithms are applied in order to
233 regenerate the mesh in the best way possible [19]. The biggest advantage of this approach is the
234 ability to resolve different scaled regions for different moments in time, thus, elements present in
235 a plastic deformation intensive region will be resized to accurately reproduce such effects.
236 Likewise, inactive areas will be coarsened, so computational resources are spared and better
237 deployed [19]. For our case, the cutting tool was modeled as a rigid body and Coulomb's friction
238 was applied to the relevant zones.
239

240 In modelling the pressure effect of coolant, the velocity of the jet was inputted to the
241 software. Which was calculated using the jet area based on the nozzle diameter, and the flow rate.
242 It is assumed that the flow is uniform and steady after leaving the nozzle and that the speed of the
243 jet is not appreciably reduced after hitting the chip. The pressure exerted by the jet is applied on
244 the chip surface. The heat exchange between the chip and coolant was modeled as convective
245 thermal boundary conditions. Orthogonal (2-dimensional) cutting was employed for simplification
246 matters, as experimental validation attested for the validity of the model, implying a plain strain
247 model that does not account for the load distribution applied by the coolant in the Z axis, and all
248 data input regarding simulation parameters are displayed in Table 1.
249

250 2.2 Experimental methodology

251

252 The cutting tests were performed on a SC-450 Nakamura-Tome CNC Lathe (Figure 2a).
253 The semi-synthetic, 6% concentrated, cutting fluid was supplied to the rake face of the
254 commercially available Kennametal CNMG 432 uncoated Tungsten Carbide (WC) grade k turning
255 insert by a ChipBLASTER J8-1000 High Pressure Coolant Supply, through Sandvik's PCLNL 16
256 4DHP (Figure 2b-c) Coolant-through tool holder.
257

258 The ASTM B265 Grade 5 Ti6Al4V workpiece (Figure 2b), also known as Ti64 was used
259 for all cutting operations. The workpiece used was of a cylindrical shape measuring approximately
260 100 mm in diameter and 250 mm in length. Material properties, chemical composition, and
261 microstructure provided by the supplier are listed in Table 2.
262

281
282
283
284 The selected cutting parameters are listed in Table 3. The main idea behind these severe
285 cutting conditions is to accelerate and intensify the wear mechanisms on the uncoated cemented
286 carbide tools. Thus, allowing for a better visualization of the phenomena taking place during the
287 cutting process, as well as the role played by the HPC supply.
288
289

290 Cutting forces were measured by a three component Kistler 9121 tool holder dynamometer
291 (2b), transmitting to a Kistler 5010 amplifier, and recorded using LABVIEW 14.0 during the first
292 50 meters of cutting length.
293

294 As shown in Figure 3, a thermocouple was positioned close to the rake face of the cutting
295 tool. The insertion was made by EDM (Electrical Discharge Machining), allowing for the
296 acquisition of peak temperature measurements [7,20]. This setup was performed exclusively for
297 modeling validation. Unaltered cutting tools were employed in the actual cutting tests.
298
299
300

301 Chips were collected at the end of the first cutting step. Therefore, tool/chip contact
302 conditions would not be affected by the geometry changes imposed by tool wear. The maximum
303 flank wear criterion was set to 300 microns or 2500 meters of cutting length, whichever occurred
304 first. Flank wear measurements were taken for 100-150-meter steps, as well as optical microscopy
305 images (KEYENCE VHX-5000) of the worn inserts' rake and flank surfaces. In order to provide
306 a better understanding of the tool/chip contact behavior during the machining process, a Tescan
307 VEGA2 Scanning Electron Microscope (SEM) was employed to acquire high magnification
308 images of surface topography of chips and worn cutting inserts. Additionally, orientation maps
309 were obtained by Electron Backscattered Diffraction (EBSD) using a JEOL JSM-7000F Scanning
310 Electron Microscope. Moreover, white light interferometry was introduced by an Alicona Infinite
311 Focus optical microscope for 3D surface measurements of the worn inserts and collected chips. A
312 high resolution Nikon Eclipse LV100 optical microscope was used for the microstructural analysis
313 of the chips' cross sections. Prior to imaging, samples were cold mounted, polished and etched by
314 swabbing a cotton ball rinsed in a solution of HF + HNO₃ for 10 seconds.
315
316
317
318
319
320
321
322

323 Vickers microhardness tests on the cross section measurements of the collected chips were
324 performed by a Matsuzawa MMT-X7A micro Vickers hardness tester with a diamond
325 quadrangular pyramid indenter at 50 gf for 10 seconds.
326
327
328
329
330
331
332
333
334
335
336

3. Results and Discussion

3.1 FEA results

As shown in Figure 4, simulation results present slightly higher temperature values in comparison to the experimental data but keeping the same trend. This difference in temperature could be attributed the thermo couple being positioned few millimetres away from the tool-chip interface [7] (Figure 3). In addition, a slight decrease in peak temperature is presented when comparing both conditions at 150 m/min (Figure 4 a,b), which can be attributed to the reduced contact pressure and consequent attenuated friction conditions occasioned by the HPC jet. While overall temperature changes are not so significant, Figure 4 (d-f) reveals a considerable difference in peak temperatures on the chips. This data indicates that a higher amount of heat is being directed towards the chip, which is a highly desirable outcome when machining difficult-to-cut alloys, since the excessive heat present at the rake face of the cutting tool will facilitate the diffusion process, resulting in accelerated crater wear and a reduction in tool life. As crater wear progresses, material is being removed from the insert, thus weakening the tool's cutting edge, ultimately leading to its catastrophic failure.

As shown in Figure 4 (e,f), the additional momentum provided by the HPC jet results in some regions of concentrated strain, where chips are most susceptible to breaking. However, the same cannot be said for the flood condition presented in Figure 4-d, where the chip curls at its natural unobstructed radius, implying an undesirable continuous chip formation that might lead to poor surface finish, excessive heat accumulation and ultimately, premature tool failure.

A notable reduction in TCCL (tool-chip contact length) for the two HPC scenarios is presented in Figure 5. The changes were ~50% for the 150 m/min (Figure 5-b) and 250 m/min (Figure 5-c) HPC conditions. The stress concentration exhibits a direct correlation with the length of the contact region. Additionally, a reduction in contact pressure is visible for the two HPC scenarios, which reflects in a less intensive overall stress profile. High contact loads are some of the main facilitators of the adhesion process, once the adhesive bond's strength is proportional to the pressure being applied to it. That said, the eventual tearing apart of the welded workpiece material will cause what is known as plucking, causing damage that is similar to the diffusion process.

393
394
395
396
397
398
399
400
401
402
403
404
405
406
407
408
409
410
411
412
413
414
415
416
417
418
419
420
421
422
423
424
425
426
427
428
429
430
431
432
433
434
435
436
437
438
439
440
441
442
443
444
445
446
447
448

The higher chip temperatures presented in Figure 4, combined with the lower contact stresses in Figure 5, indicate an increase in the portion of heat generated by plastic deformation over the heat provided by friction for the HPC conditions.

3.2 Tool life

Figure 6 presents a direct tool life comparison between all the tested conditions. The graph shows the maximum flank wear achieved at the same cutting length (as displayed on the graph) for each set of cutting parameters proposed in Table 3. The length is determined by the point of failure (when flank wear exceeds the pre-established end of life criteria) for the worst performing coolant pressure at a specific cutting speed.

When analysing the results presented in Figure 6, a trend can be noticed in terms of maximum flank wear vs. coolant pressure. Higher coolant pressures have a positive impact on wear rates throughout the cutting process, which can be attributed to the reduced thermal and mechanical loads acting on the tool, as seen in Figures 4 and 5. Hoier et al. [21] highlighted similar behavior when machining Inconel 718 with HPC supply. This was attributed to the cobalt binder present in the insert's composition being subject to thermal softening, making it easier to be removed in the abrasion process. The temperature profiles shown in Figure 4 support that idea. For the flood condition, heat is being dissipated into the cutting tool instead of being carried away by the chips. Furthermore, it also explains the higher flank wear rates measured for the cutting speeds of 200 m/min and 250 m/min.

As shown in Figure 7, when cutting at the lowest speed of 150 m/min with the addition of HPC, inserts were able to reach 2500 meters of cutting length without surpassing the pre-established end of life criteria (300 μm flank wear). In fact, when looking at the wear curves shown in Figure 7, flank wear was less than half of what was obtained for the flood benchmark condition. Similar results were obtained at the highest cutting speed of 250 m/min, where the best tool life results were achieved for the same pressure of 1000 psi.

Cutting forces (Figure 8) are also significantly lower for the HPC when compared to the benchmark. A reduction in the order of 40% at 150 m/min can be observed, which can be attributed to a more efficient chip evacuation, thus requiring less power from the machine tool to advance the cut. A correlation can also be established between the stress profiles seen in Figure 5 and the cutting forces in Figure 8, once the compressive loads acting against the cutting movement are

449
450
451 visibly higher for the flood condition. On that basis, cutting forces are mainly dependant on the
452 area of the shear planes [7,22]. Hence, the reduction in TCCL has a direct impact on the values
453 observed for the two HPC scenarios. These results agree to what was found by previous research
454 performed by Jagtap et al. [23]. On that premise, further analyses were narrowed down to the
455 benchmark flood condition and these two sets of parameters: 150 m/min at 1000 psi and 250 m/min
456 at 1000 psi. With the focus on pointing out the factors leading to this notable improvement in tool
457 wear and cutting forces.
458
459
460
461
462

463 3.3 Tool wear modes and mechanisms 464

465 Secondary Electron SEM images were taken from the worn tools' rake and flank faces in
466 order to identify the main wear modes taking place during the cutting process. When analysing
467 Figure 9 (a-c), the dominance of adhesion and diffusion over other wear mechanisms becomes
468 evident, what leads to the formation of Built-up edge (BUE) and crater wear modes. The images
469 also show a positive influence of cutting speed on the BUE formation [7,22,24]. In Figure 9-a, the
470 extension of crater wear is about double the size of what is seen at the same cutting speed for the
471 HPC condition (Figure 9-b), supporting a shorter contact length. The presence of oxidation wear
472 is only expressive for the flood condition (Figure 9-a). Oxidation is normally found near the end
473 of the contact region, being a result of the reaction between oxygen and the tool binder [7]. On that
474 premise, the less intense sliding contact pressure, present in that area, allows for the access of
475 oxygen; thus, enabling the reaction. Furthermore, abrasion marks were noticed to be more
476 pronounced at the high-speed condition presented in Figure 9-c, resulting in lower tool life.
477 Abrasion is visible since there is not a substantial volume of material adhered to the rake face of
478 the insert.
479
480
481
482
483
484
485
486
487

488 Further volumetric analysis showed that for both HPC (Figure 10) scenarios the amount of
489 adhered material, represented by V_p (Volume of peaks above reference), is in fact reduced (Figure
490 10 b,c) when compared to the flood condition. It also displays the lower adhesion at a higher
491 cutting speed (Figure 10-c). In contrast to that, V_v (Volume of valleys below reference),
492 representing the volume of removed tool material, is noticeably higher at this speed. Note that this
493 number accounts not only for crater wear, but also for the abrasion that is very pronounced at 250
494 m/min.
495
496
497
498
499
500
501
502
503
504

505
506
507
508
509
510
511
512
513
514
515
516
517
518
519
520
521
522
523
524
525
526
527
528
529
530
531
532
533
534
535
536
537
538
539
540
541
542
543
544
545
546
547
548
549
550
551
552
553
554
555
556
557
558
559
560

There are three main contributors to the presented wear mechanisms: contact, load and affinity. In this way, HPC promotes the separation between the chip and the rake face of the cutting tool, thus reducing the contact length as well as the mechanical loads acting on that region, which can be proven by the simulation results shown in Figures 4 and 5.

3.4 Cutting chips analysis

Secondary electron images of the chips undersurface and shear bands were taken to attest for the influence of HPC on chip morphology. By looking at the undersurface of the studied chips (Figure 11-a), some inclusions are noticed to be more frequent at the HPC scenarios, which is possibly an indicator of the sticky nature of contact for those conditions. To strengthen that hypothesis, as previously observed in Figure 9, a longer sliding contact region was detected for the benchmark flood scenario, which means reduced contact pressure at the tool / chip interface.

Images shown in Figure 11-b have revealed that segmentation is present for all three of the tested conditions. In general, segmented chips are common when machining alloys with high hardness and low thermal conductivity, such as titanium [25]. It is also considered, for some particular situations, a desirable outcome for cutting force reduction and enhanced chip evacuation [26]. Furthermore, the segmentation edges are smoother when working with the high-pressure coolant supply, meaning that the shear band formation process is facilitated by its application, revealing one of the possible reasons for the force reductions presented in Figure 8. Tool wear will also impact the chip formation process, as stated by Dargusch et al. [25], segmentation and deformation of chips will be significantly impacted as machining progresses.

Based on the obtained experimental results for chip formation and tool wear mechanisms, the schematic diagram presented in Figure 12 attempts to illustrate the changes occurring at the tool/chip contact area when applying HPC. In Figure 12-a, the normal stress decreases exponentially along the contact region and is inversely proportional to the chip's sliding velocity, becoming maximum at the tool tip and minimum at the point where chip loses contact with the cutting tool. The normal stress and sliding velocity profiles combined, contribute to the definition of the so-called sticking and sliding regions, the first one being characterized by high levels of contact pressure and significantly low chip sliding velocity, and the second one where pressure is reduced, thus allowing the chip to flow at a higher speed. These contact conditions are altered once HPC is introduced. As presented in Figure 12-b, once contact pressure (normal stress) is reduced

561
562
563
564 to a certain level, by the application of high-pressure coolant, the chip immediately loses contact
565 with the tool's rake face, not allowing for the sliding interaction. On that basis, a direct correlation
566 can be drawn from the tools analyzed in Figure 9, where oxidation was not significant for the HPC
567 conditions; therefore, suggesting a substantially shorter low pressure contact area, and the chips
568 presented in Figure 11, where the presence of inclusions on the collected samples, characterizes a
569 process of "sticky" nature.
570
571
572

573 To investigate the role of HPC as well as the cutting speeds on the shear bands, the chip
574 cross sections were analyzed using EBSD, and the acquired data is presented in Figure 13. As
575 shown, the resulting orientation maps of the regions taken from the chips in Figure 13 (a, c, e) are
576 shown in Figure 13 (b, d, f), respectively. It can be observed that the grains are more elongated at
577 higher cutting speeds (Figure 13-f) when compared to lower ones (Figure 13-d). The same can be
578 stated when comparing HPC to flood conditions, because of the severe plastic deformation caused
579 by HPC application. Here, the shear bands formed by flood coolant (Figure 13-b) have equiaxed
580 grains (~1 μm) compared to a mixture of equiaxed (~7 μm) and highly elongated grains in the case
581 of machining with HPC (Figure 13 (d, f)).
582
583
584
585
586

587 Figure 14 presents the pole Figure maps of the chips obtained at different cutting
588 conditions. As shown, most of the grains in the chips obtained with flood condition, possess a Goss
589 $\{1\ 1\ 0\}$ texture (Figure 14-a) while the majority of the grains obtained with HPC possess an
590 orientation close to the Cube $\{1\ 0\ 0\}$ (001) texture as shown in Figure 14-b and 14-c. Seid Ahmed
591 et al. [27] concluded that in general, the Cube texture has higher plasticity compared to the Goss
592 texture. The main reason for this is that the Cube texture contains more slip systems, helping it to
593 deform quickly during the machining process [28]. Thus, the chips obtained with HPC (Figures
594 14-b and 14-c) show highly elongated grains compared with very equiaxed grains of the chips
595 obtained with flood condition.
596
597
598
599
600

601 The micro hardness values in Table 4 are in agreement with the EBSD data presented in
602 Figures 13 and 14, attesting for the strain hardening resultant of the high deformation levels
603 imposed by the application of HPC. This becomes more evident for the areas close to the tool-chip
604 contact region, where the variation in hardness is noticeably higher. The severe plastic deformation
605 imposed by HPC causes the chips to strain harden, and once they are fragilized, their breakability
606 is improved.
607
608
609
610

4. Conclusions

The experiments performed showed that the tool-chip contact conditions are affected significantly by the application of HPC, indicating that its influence goes beyond chip control. It also allowed for the establishment of a correlation between: coolant pressure, cutting speed, tool life, cutting forces, wear mechanisms, and chip formation. Resulting in the following contributions:

1. Modeling and experiments show a tool temperature reduction for the HPC process, whereas for these same conditions, peak chip temperatures are increased. This data combined with the less severe tool-chip interactions demonstrated in the stress profiles, indicates an increase in the portion of heat generated by plastic deformation over the heat provided by friction for the HPC conditions. In addition, it also results in reduced diffusion and adhesion rates.
2. Coolant pressure and maximum flank wear are inversely proportional to each other, indicating an influence of the heat directed towards the flank face of the cutting tool on the abrasion process. This fact could be explained by the thermal softening of the cobalt binder present in the insert's composition.
3. Oxidation wear is noticeably less extensive when employing HPC supplies, which suggests an interruption of tool-chip contact right after the end of the sticking zone.
4. Chip formation is facilitated by HPC. Improved chip evacuation allied to the lower compressive loads at the rake face of the cutting insert, caused a reduction in cutting forces as well as the formation of smoother shear bands, indicating a more stable process.
5. The strain hardening of the chips collected for the HPC process have a positive impact on their breakability. This fact is supported by the EBSD results, which attested for the presence of highly deformed grain textures.

Acknowledgements

The authors gratefully acknowledge that this research was supported by Natural Sciences and Engineering Research Council of Canada (NSERC) under the CANRIMT Strategic Research Network Grant NETGP 479639-15.

673
674
675
676
677 **References**
678

- 679
680 [1] Lütjerin G, Williams JC. Titanium. Berlin, Heidelberg: Springer; 2007. doi:10.1007/978-3-
681 540-73036-1.
682
683
684 [2] Veiga C., Devim J. P., Loureiro A. J. R. Properties and applications of titanium alloys: a
685 brief review. Rev Adv Mater Sci 2012;32:133–48.
686
687
688
689 [3] Ezugwu EO, Batista Da Silva R, Falco Sales W, Rocha Machado A. Overview of the
690 Machining of Titanium Alloys. Encycl. Sustain. Technol., vol. 2, Elsevier; 2017, p. 487–
691 506. doi:10.1016/B978-0-12-409548-9.10216-7.
692
693
694
695
696 [4] Ezugwu EO. Key improvements in the machining of difficult-to-cut aerospace superalloys.
697 Int J Mach Tools Manuf 2005;45:1353–67. doi:10.1016/j.ijmachtools.2005.02.003.
698
699
700
701 [5] Guo YB, Li W, Jawahir IS. Surface integrity characterization and prediction in machining
702 of hardened and difficult-to-machine alloys: A state-of-art research review and analysis.
703 Mach Sci Technol 2009;13:437–70. doi:10.1080/10910340903454922.
704
705
706
707
708 [6] Rosemar B, Machado ÁR, Ezugwu EO, Bonney J, Sales WF. Journal of Materials
709 Processing Technology Tool life and wear mechanisms in high speed machining of Ti – 6Al
710 – 4V alloy with PCD tools under various coolant pressures 2013;213:1459–64.
711
712
713
714
715 [7] Shaw MC. Metal Cutting Principles. New York: Oxford University Press; 2002.
716 doi:10.1016/0025-5408(96)80018-3.
717
718
719
720 [8] Paiva JM, Shalaby MAM, Chowdhury M, Shuster L, Chertovskikh S, Covelli D, et al.
721 Tribological and Wear Performance of Carbide Tools with TiB₂ PVD Coating under
722
723
724
725
726
727
728

- 729
730
731 Varying Machining Conditions of TiAl6V4 Aerospace Alloy. *Coatings* 2017;7:187.
732
733 doi:10.3390/coatings7110187.
734
735
- [9] Chowdhury MSI, Chowdhury S, Yamamoto K, Beake BD, Bose B, Elfizy A, et al. Wear
736 behaviour of coated carbide tools during machining of Ti6Al4V aerospace alloy associated
737 with strong built up edge formation. *Surf Coatings Technol* 2017;313:319–27.
738
739 doi:10.1016/j.surfcoat.2017.01.115.
740
741
- [10] Liu W, Liu Z. High-pressure coolant effect on the surface integrity of machining titanium
742 alloy Ti-6Al-4V: a review. *Mater Res Express* 2018;5:032001. doi:10.1088/2053-
743 1591/aab44f.
744
745
- [11] Suhaimi MA, Yang G-D, Park K-H, Hisam MJ, Sharif S, Kim D-W. Effect of Cryogenic
746 Machining for Titanium Alloy Based on Indirect, Internal and External Spray System.
747 *Procedia Manuf* 2018;17:158–65. doi:10.1016/j.promfg.2018.10.031.
748
749
- [12] Park K-H, Yang G-D, Suhaimi MA, Lee DY, Kim T-G, Kim D-W, et al. The effect of
750 cryogenic cooling and minimum quantity lubrication on end milling of titanium alloy Ti-
751 6Al-4V. *J Mech Sci Technol* 2015;29:5121–6. doi:10.1007/s12206-015-1110-1.
752
753
- [13] Khatri A, Jahan MP. Investigating tool wear mechanisms in machining of Ti-6Al-4V in
754 flood coolant, dry and MQL conditions. *Procedia Manuf* 2018;26:434–45.
755
756 doi:10.1016/j.promfg.2018.07.051.
757
758
- [14] Attanasio A, Gelfi M, Giardini C, Remino C. Minimal quantity lubrication in turning: Effect
759 on tool wear. *Wear* 2006;260:333–8. doi:10.1016/j.wear.2005.04.024.
760
761
- [15] Klocke F, Lung D, Cayli T, Döbbeler B, Sangermann H. Evaluation of energy efficiency in
762
763
764
765
766
767
768
769
770
771
772
773
774
775
776
777
778
779
780
781
782
783
784

- 785
786
787 cutting aerospace materials with high-pressure cooling lubricant supply. *Int J Precis Eng*
788 *Manuf* 2014;15:1179–85. doi:10.1007/s12541-014-0454-2.
789
790
791
- [16] Vakis AI, Yastrebov VA, Scheibert J, Nicola L, Dini D, Minfray C, et al. Modeling and
792 simulation in tribology across scales: An overview. *Tribol Int* 2018;125:169–99.
793 doi:10.1016/j.triboint.2018.02.005.
794
795
796
797
- [17] Melkote SN, Grzesik W, Outeiro J, Rech J, Schulze V, Attia H, et al. Advances in material
798 and friction data for modelling of metal machining. *CIRP Ann* 2017;66:731–54.
799 doi:10.1016/j.cirp.2017.05.002.
800
801
802
803
804
805
- [18] Liu C, Goel S, Llavori I, Stolf P, Giusca CL, Zabala A, et al. Benchmarking of several
806 material constitutive models for tribology, wear, and other mechanical deformation
807 simulations of Ti6Al4V. *J Mech Behav Biomed Mater* 2019;97:126–37.
808 doi:10.1016/j.jmbbm.2019.05.013.
809
810
811
812
813
814
- [19] Man X, Ren D, Usui S, Johnson C, Marusich TD. Validation of Finite Element Cutting
815 Force Prediction for End Milling. *Procedia CIRP* 2012;1:663–8.
816 doi:10.1016/j.procir.2012.05.019.
817
818
819
820
821
- [20] Komanduri R, Hou Z. A review of the experimental techniques for the measurement of heat
822 and temperatures generated in some manufacturing processes and tribology. *Tribol Int*
823 2001;34:653–82. doi:10.1016/S0301-679X(01)00068-8.
824
825
826
827
828
- [21] Hoier P, Klement U, Tamil Alagan N, Beno T, Wretland A. Flank wear characteristics of
829 WC-Co tools when turning Alloy 718 with high-pressure coolant supply. *J Manuf Process*
830 2017;30:116–23. doi:10.1016/j.jmapro.2017.09.017.
831
832
833
834
835
836
837
838
839
840

- 841
842
843 [22] Trent EM. Metal Cutting. London: Butterworths; 1983.
844
845
846 [23] Jagtap KA, Pawade RS. Some Studies on Chip Formation Mechanism in CNC Turning of
847
848 Biocompatible Co-Cr-Mo Alloy. Procedia Manuf 2018;20:283–9.
849
850 doi:10.1016/j.promfg.2018.02.042.
851
852
853 [24] Oliaei SNB, Karpat Y. Built-up edge effects on process outputs of titanium alloy micro
854
855 milling. Precis Eng 2017;49:305–15. doi:10.1016/j.precisioneng.2017.02.019.
856
857
858 [25] Dargusch MS, Sun S, Kim JW, Li T, Trimby P, Cairney J. Effect of tool wear evolution on
859
860 chip formation during dry machining of Ti-6Al-4V alloy. Int J Mach Tools Manuf
861
862 2018;126:13–7. doi:10.1016/j.ijmachtools.2017.12.003.
863
864
865 [26] Chandra A, Karra P, Bragg A, Wang J, Kim GY. Chip Segmentation in Machining: A Study
866
867 of Deformation Localization Characteristics in Ti6Al4V. Vol. 1 Process., ASME; 2013.
868
869 doi:10.1115/MSEC2013-1070.
870
871
872 [27] Ahmed YS, Paiva JM, Bose B, Veldhuis SC. New observations on built-up edge structures
873
874 for improving machining performance during the cutting of superduplex stainless steel.
875
876 Tribol Int 2019;137:212–27. doi:10.1016/j.triboint.2019.04.039.
877
878
879 [28] Nomani J, Pramanik A, Hilditch T, Littlefair G. Stagnation Zone during the Turning of
880
881 Duplex SAF 2205 Stainless Steels Alloy. Mater Manuf Process 2017.
882
883 doi:10.1080/10426914.2017.1279289.
884
885
886
887

888 **List of figures**

889
890
891
892
893
894
895
896

897
898
899 **Fig. 1.** – Graphic representation highlighting the changes in chip formation and contact length
900 between (a) flood/dry and (b) HPC conditions.
901

902
903 **Fig. 2.** (a) Machine tool, (b) workpiece, dynamometer, tool holder setup and (c) detailed view of
904 tool and coolant-through tool holder.
905

906
907 **Fig. 3.** Experimental temperature measurement point.
908

909 **Fig. 4.** Temperature measurements for both simulation and experimental conditions, combined
910 with FEA results for chip formation at (a,d) flood – 150 m/min, (b,e) 1000 psi – 150 m/min and
911 (c,f) 1000 psi – 250 m/min.
912

913
914 **Fig. 5.** Tool stress profiles and TCCL for (a) flood – 150 m/min, (b) 1000 psi – 150 m/min and
915 (c) 1000 psi – 250 m/min.
916

917
918 **Fig. 6.** Flank wear comparison chart + MRR (Material Removal Rates) for all conditions.
919

920
921 **Fig. 7.** Tool wear progression curves for flood – 150 m/min, 1000 psi – 150 m/min and 1000 psi
922 – 250 m/min.
923

924
925 **Fig. 8.** Cutting forces for flood – 150 m/min, 1000 psi – 150 m/min and 1000 psi – 250 m/min.
926

927 **Fig. 9.** SEM of worn inserts for (a) flood – 150 m/min, (b) 1000 psi – 150 m/min and (c) 1000
928 psi – 250 m/min, indicating the presence of oxidation, crater, BUE and flank wear modes.
929

930
931 **Fig. 10.** Volumetric analysis of worn tools for (a) flood – 150 m/min, (b) 1000 psi – 150 m/min
932 and (c) 1000 psi – 250 m/min, indicating the volumes of adhered and removed material from the
933 cutting inserts.
934

935
936 **Fig. 11.** SEM of (a) chip undersurfaces and (b) shear bands.
937

938 **Fig. 12.** Tribological conditions along the rake face of the insert for (a) dry / flood, and (b) high-
939 pressure coolant conditions.
940

941
942 **Fig. 13.** Chips cross-sections and EBSD orientation maps for (a,b) flood – 150 m/min, (c,d) 1000
943 psi – 150 m/min and (e,f) 1000 psi – 250 m/min.
944

945
946 **Fig. 14.** EBSD pole figures for (a) flood – 150 m/min, (b) 1000 psi – 150 m/min and (c) 1000 psi
947 – 250 m/min.
948

953
954
955 **List of tables**
956

957
958 **Table 1.** Simulation parameters for all the tested conditions.
959

960 **Table 2.** Chemical Composition, and main mechanical properties of Ti-6Al-4V at room
961 temperature.
962

963
964 **Table 3.** Machining parameters for experimental testing.
965

966 **Table 4.** Shear band chips microhardness profiles for flood – 150 m/min, 1000 psi – 150 m/min
967 and 1000 psi – 250 m/min with values highlighted for the points located near the tool-chip
968 interface.
969
970
971
972
973
974
975
976
977
978
979
980
981
982
983
984
985
986
987
988
989
990
991
992
993
994
995
996
997
998
999
1000
1001
1002
1003
1004
1005
1006
1007
1008

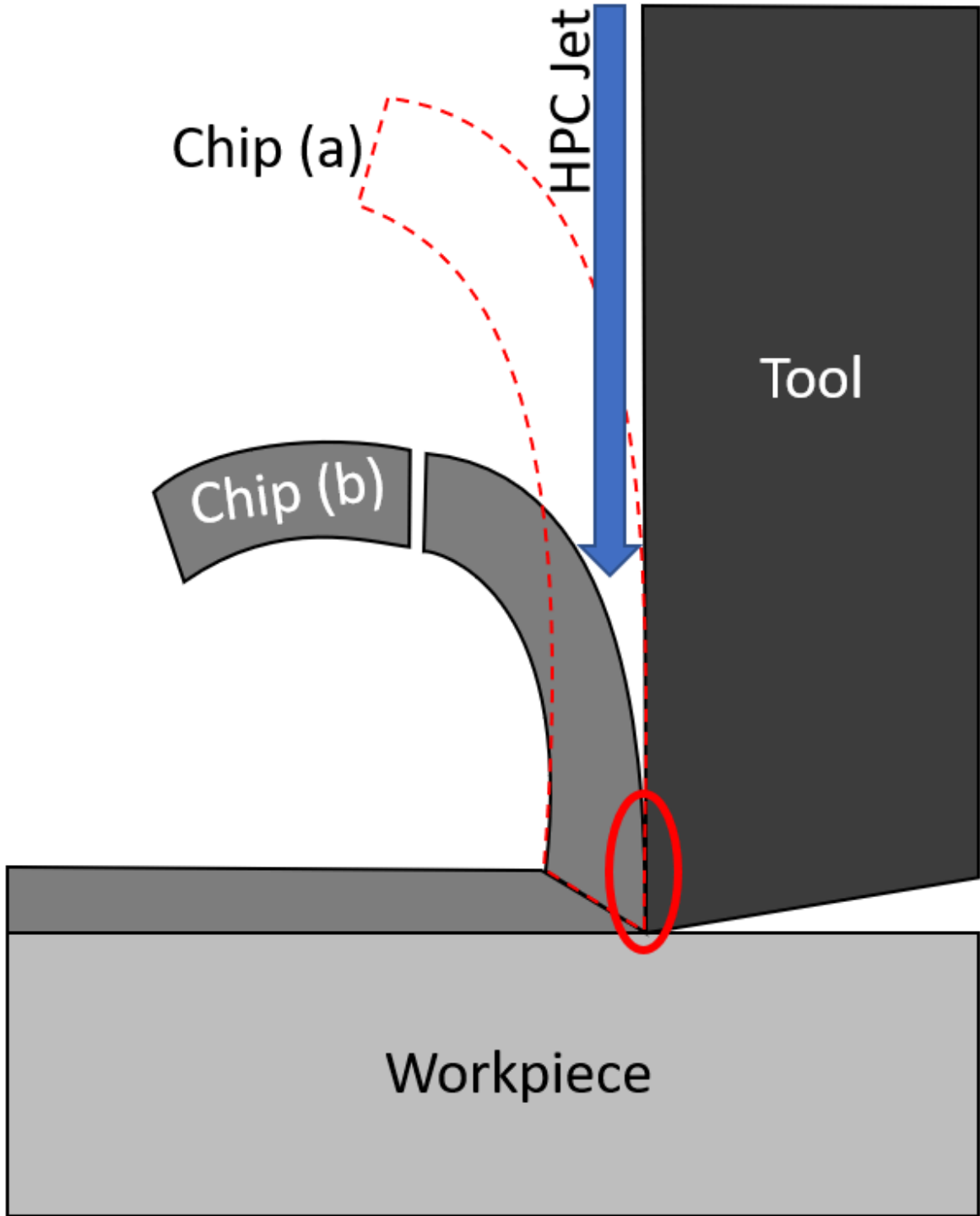
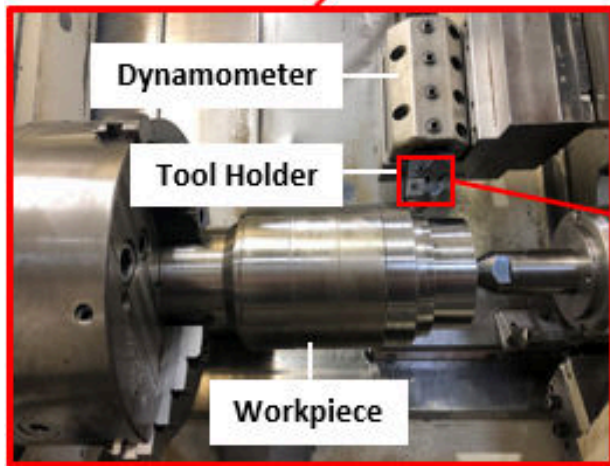


Fig. 1. – Graphic representation highlighting the changes in chip formation and contact length between (a) flood/dry and (b) HPC conditions.

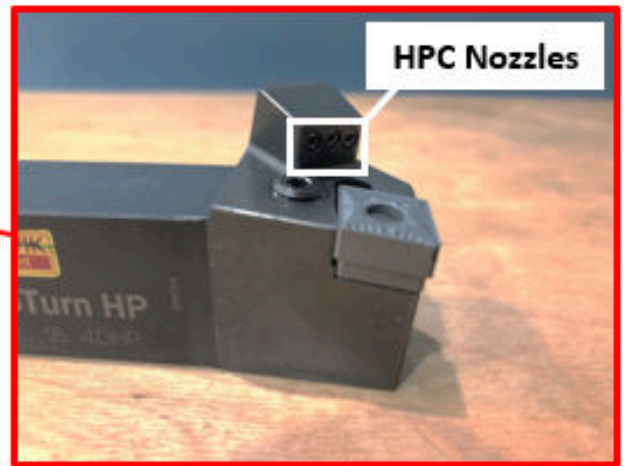
57
58
59
60
61
62
63
64
65
66
67
68
69
70
71
72
73
74
75
76
77
78
79
80
81
82
83
84
85
86
87
88
89
90
91
92
93
94
95
96
97
98
99
100
101
102
103
104
105
106
107
108
109
110
111
112



(a)



(b)



(c)

Fig. 2. – (a) Machine tool, (b) workpiece, dynamometer, tool holder setup and (c) detailed view of tool and coolant-through tool holder.

113
114
115
116
117
118
119
120
121
122
123
124
125
126
127
128
129
130
131
132
133
134
135
136
137
138
139
140
141
142
143
144
145
146
147
148
149
150
151
152
153
154

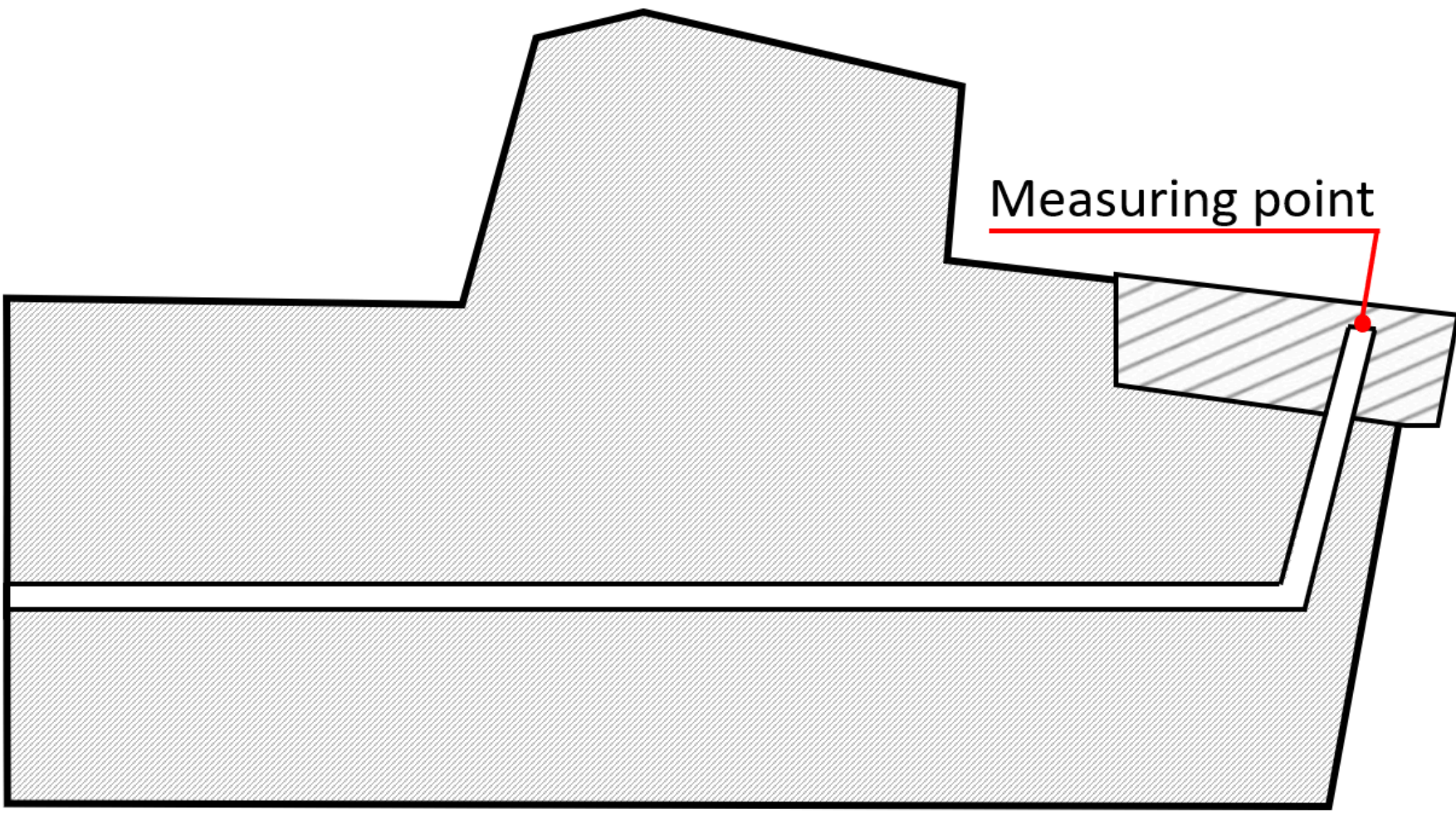


Fig. 3. – Experimental temperature measurement point.

155
156
157
158
159
160
161
162
163
164
165
166
167
168
169
170
171
172
173
174
175
176
177
178
179
180
181
182
183
184
185
186
187
188
189
190
191
192
193
194
195
196

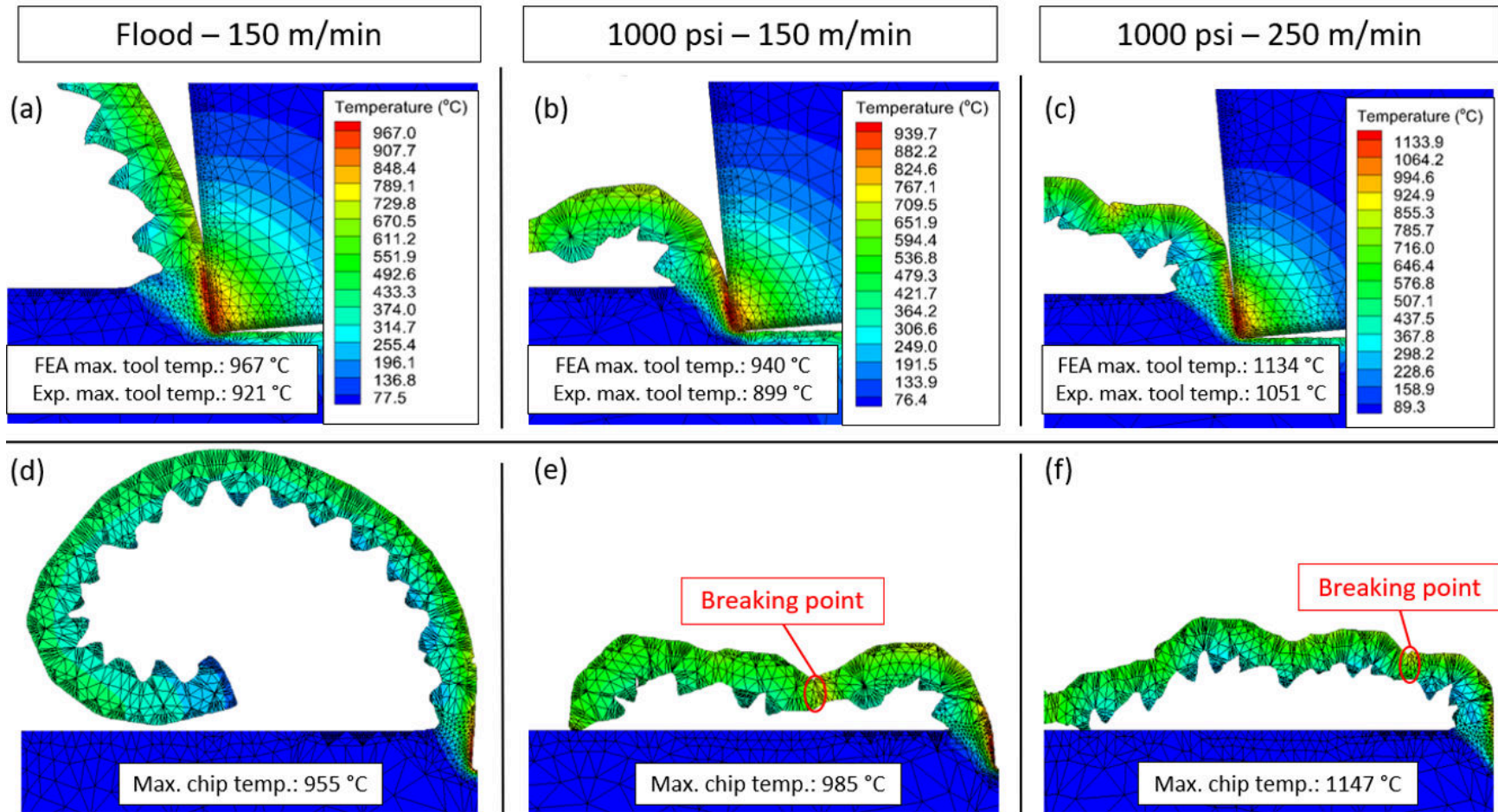


Fig. 4. – Temperature measurements for both simulation and experimental conditions, combined with FEA results for chip formation at (a,d) flood – 150 m/min, (b,e) 1000 psi – 150 m/min and (c,f) 1000 psi – 250 m/min.

197
198
199
200
201
202
203
204
205
206
207
208
209
210
211
212
213
214
215
216
217
218
219
220
221
222
223
224
225
226
227
228
229
230
231
232
233
234
235
236
237
238

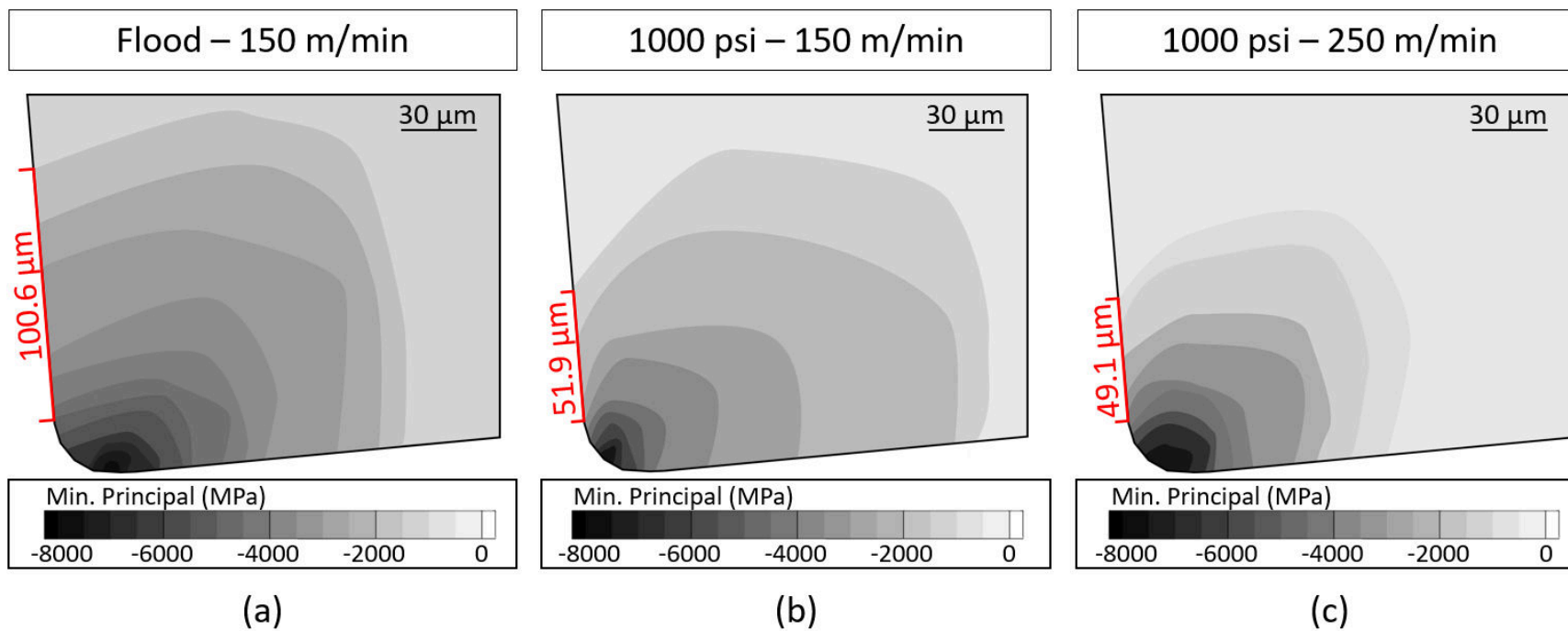


Fig. 5. – Tool stress profiles and TCCL for (a) flood – 150 m/min, (b) 1000 psi – 150 m/min and (c) 1000 psi – 250 m/min.

239
240
241
242
243
244
245
246
247
248
249
250
251
252
253
254
255
256
257
258
259
260
261
262
263
264
265
266
267
268
269
270
271
272
273
274
275
276
277
278
279
280

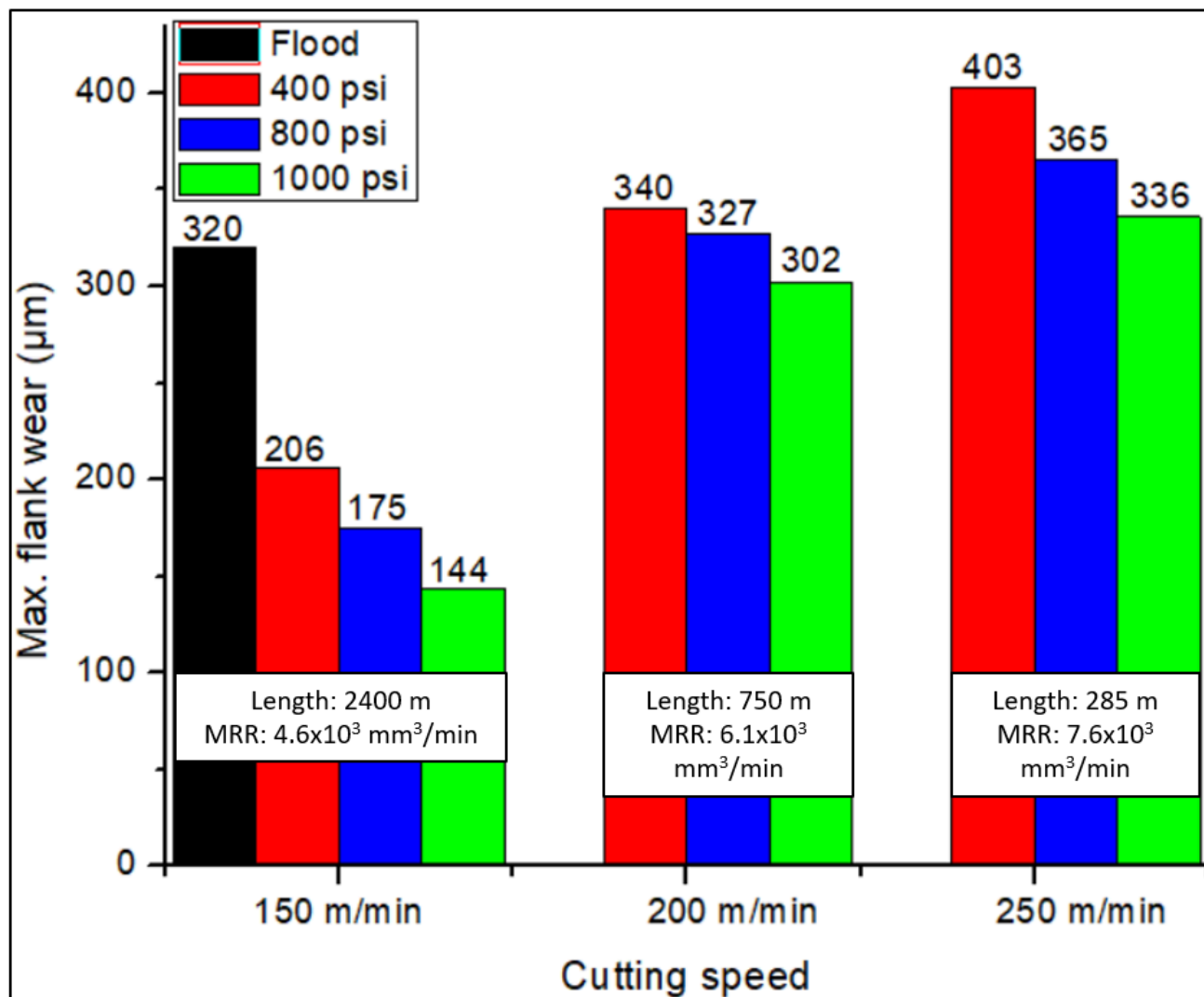


Fig. 6. – Flank wear comparison chart + MRR (Material Removal Rates) for all conditions.

281
282
283
284
285
286
287
288
289
290
291
292
293
294
295
296
297
298
299
300
301
302
303
304
305
306
307
308
309
310
311
312
313
314
315
316
317
318
319
320
321
322

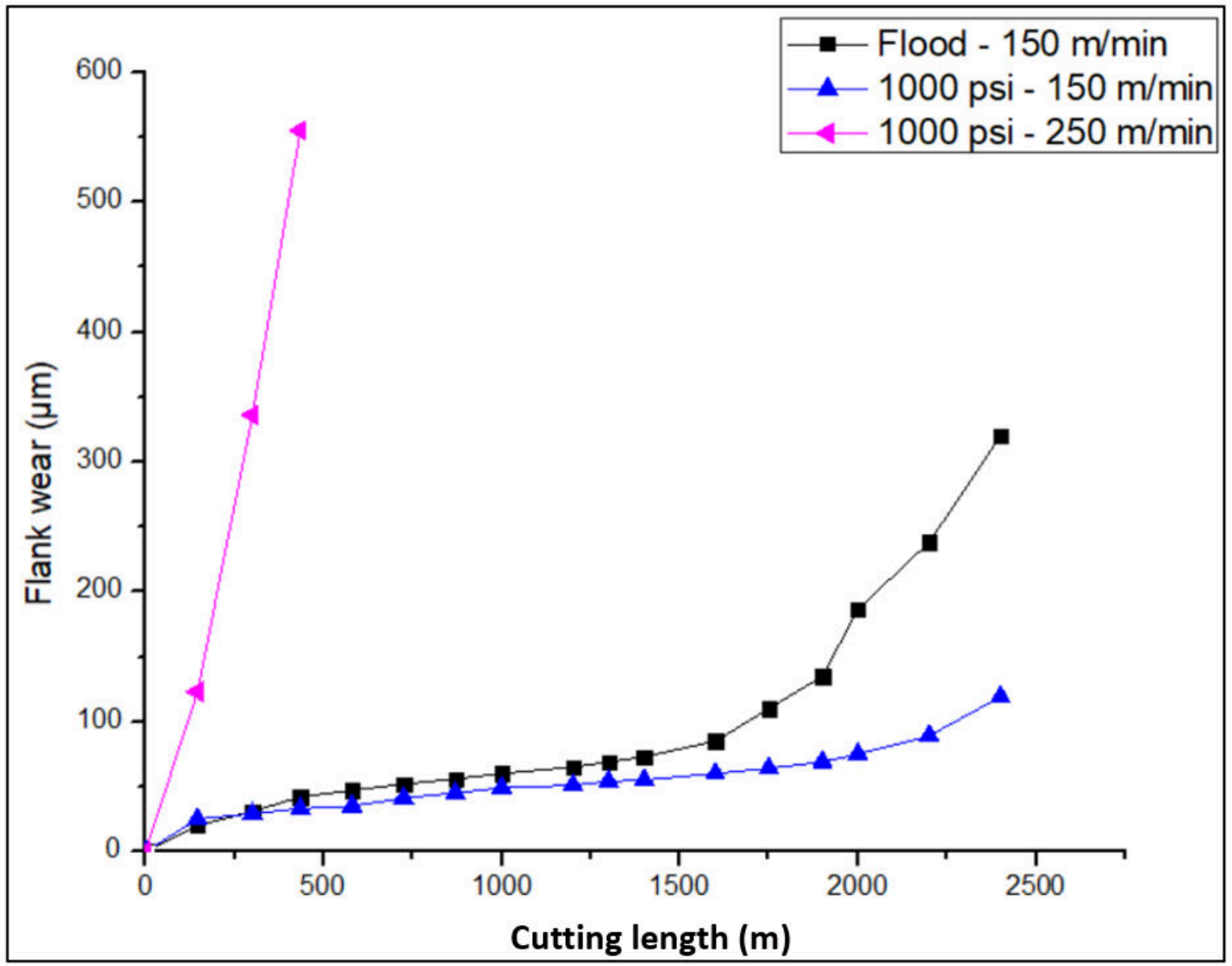


Fig. 7. – Tool wear progression curves for flood – 150 m/min, 1000 psi – 150 m/min and 1000 psi – 250 m/min.

323
324
325
326
327
328
329
330
331
332
333
334
335
336
337
338
339
340
341
342
343
344
345
346
347
348
349
350
351
352
353
354
355
356
357
358
359
360
361
362
363
364

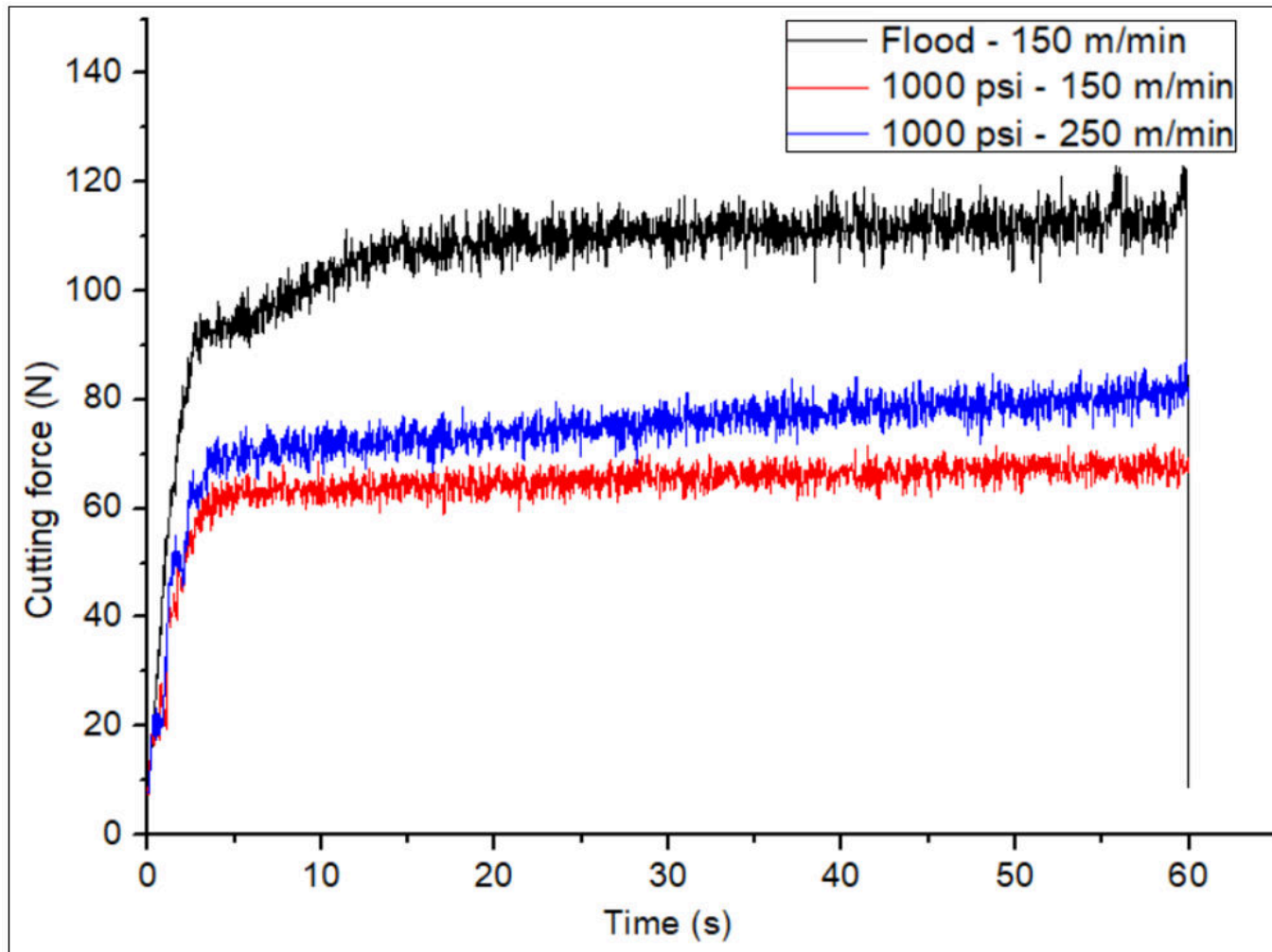


Fig. 8. – Cutting forces for flood – 150 m/min, 1000 psi – 150 m/min and 1000 psi – 250 m/min.

365
366
367
368
369
370
371
372
373
374
375
376
377
378
379
380
381
382
383
384
385
386
387
388
389
390
391
392
393
394
395
396
397
398
399
400
401
402
403
404
405
406

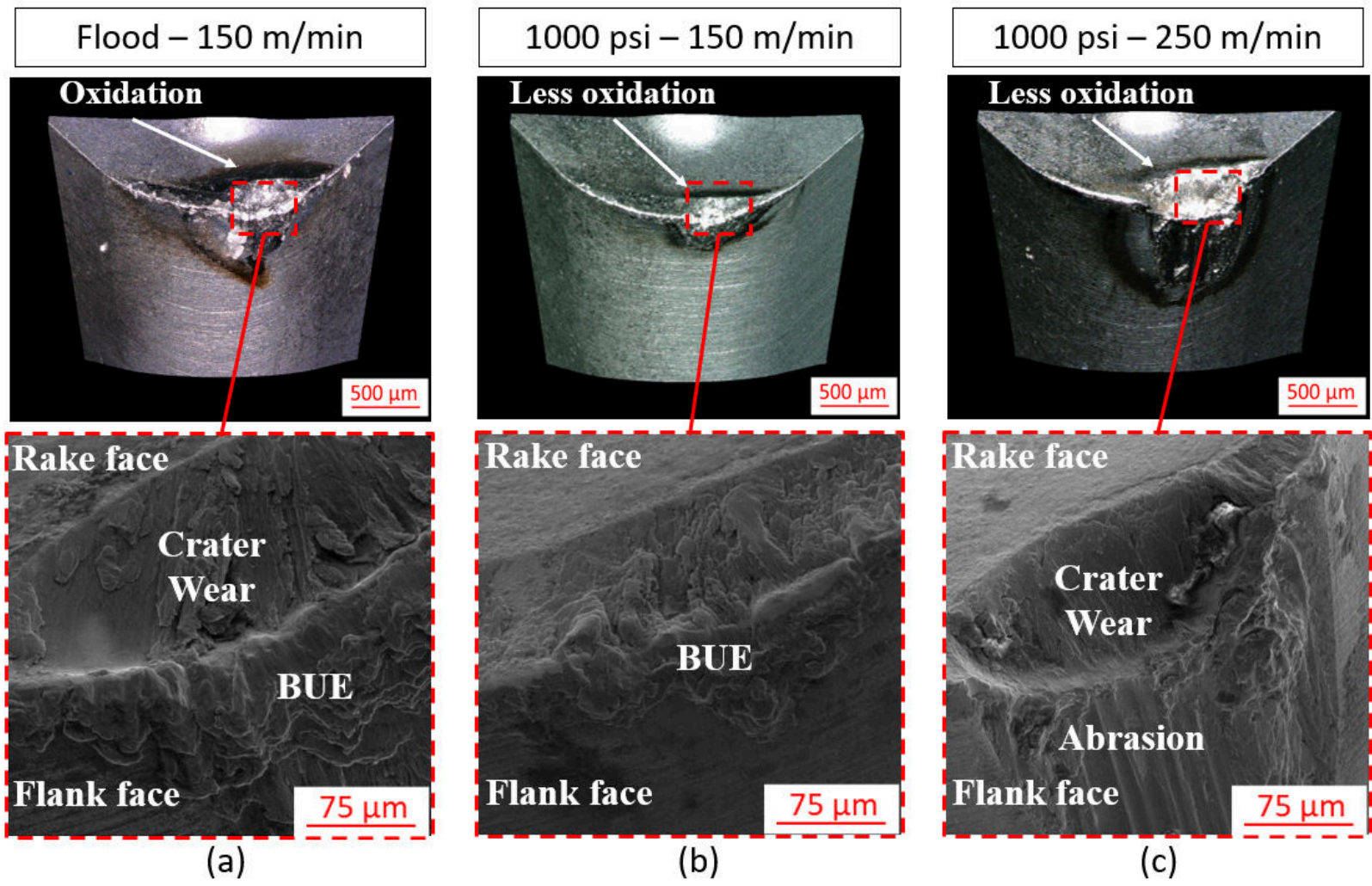


Fig. 9. – SEM of worn inserts for (a) flood – 150 m/min, (b) 1000 psi – 150 m/min and (c) 1000 psi – 250 m/min, indicating the presence of oxidation, crater, BUE and flank wear modes.

407
408
409
410
411
412
413
414
415
416
417
418
419
420
421
422
423
424
425
426
427
428
429
430
431
432
433
434
435
436
437
438
439
440
441
442
443
444
445
446
447
448

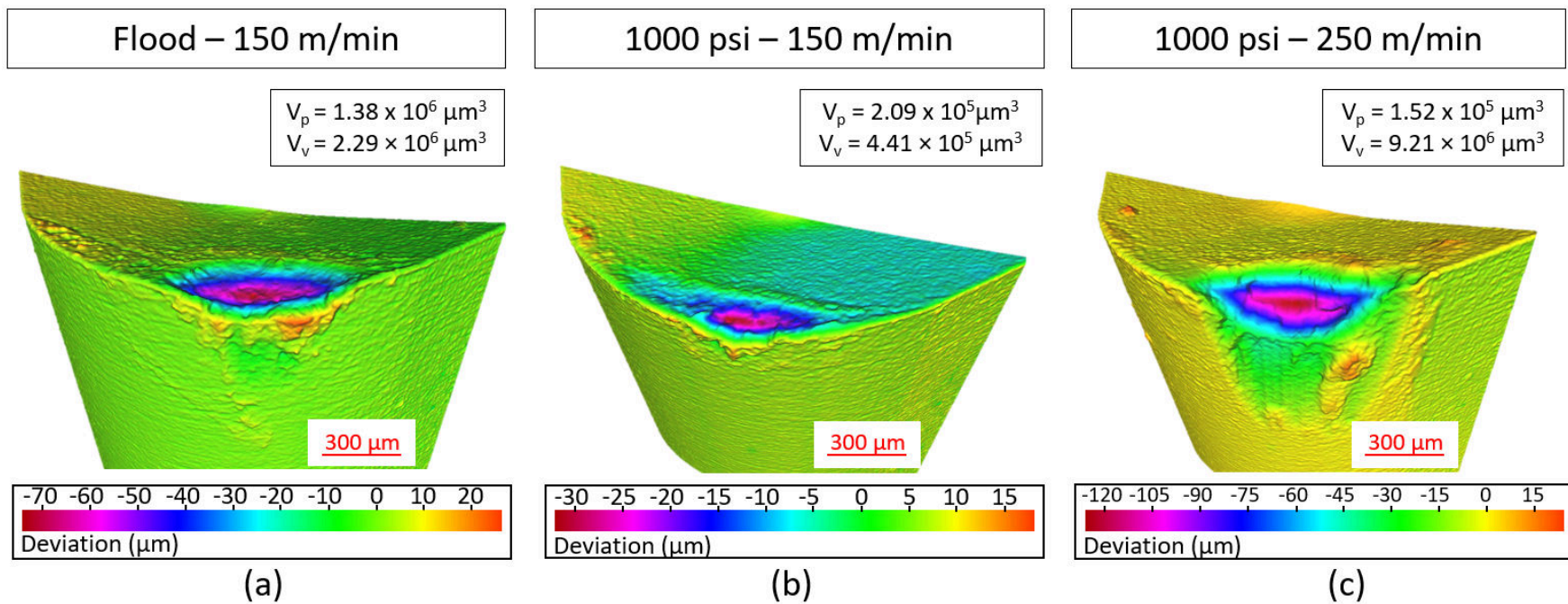


Fig. 10. – Volumetric analysis of worn tools for (a) flood – 150 m/min, (b) 1000 psi – 150 m/min and (c) 1000 psi – 250 m/min, indicating the volumes of adhered and removed material from the cutting inserts.

449
450
451
452
453
454
455
456
457
458
459
460
461
462
463
464
465
466
467
468
469
470
471
472
473
474
475
476
477
478
479
480
481
482
483
484
485
486
487
488
489
490

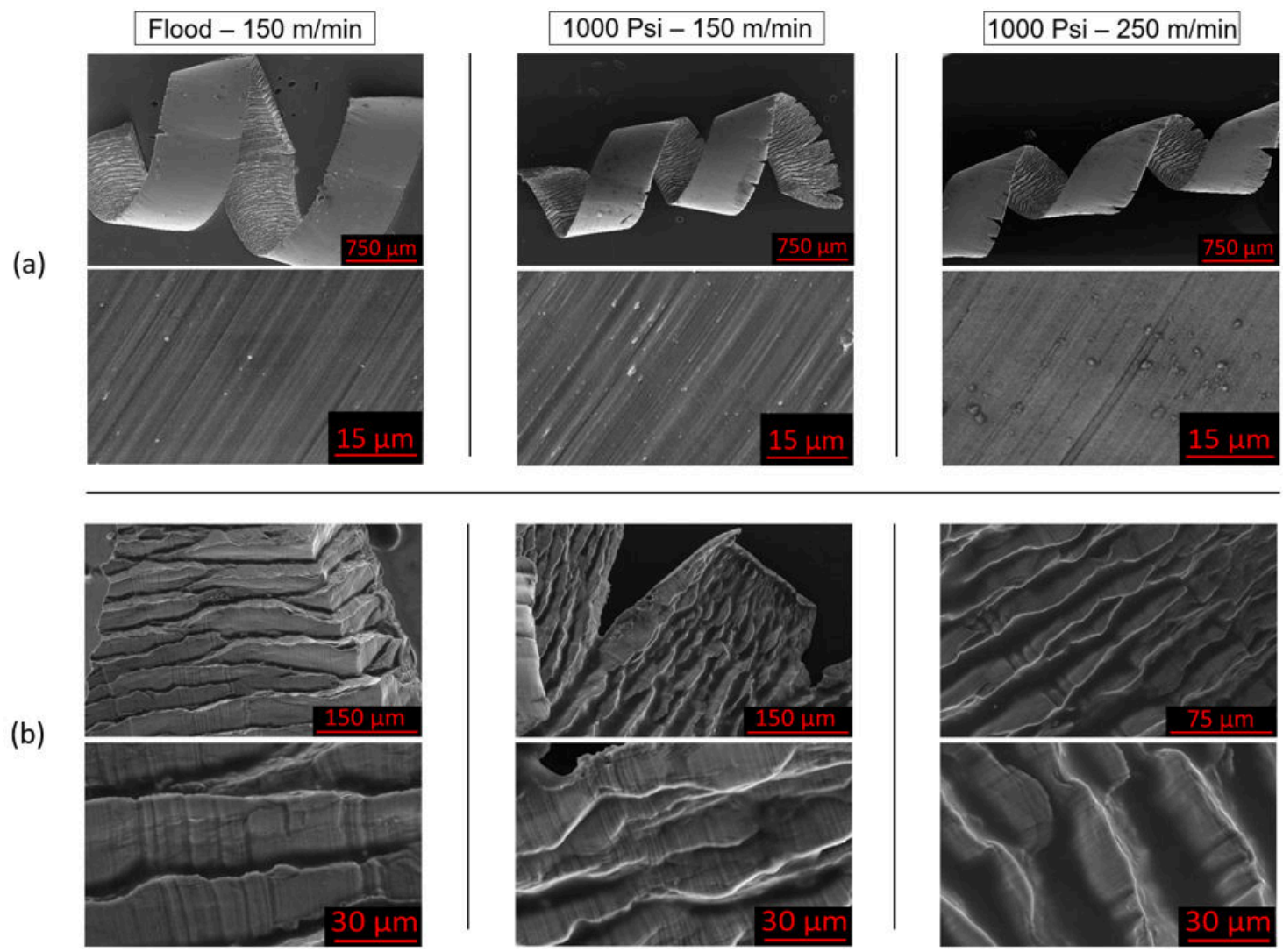


Fig. 11. – SEM of (a) chip undersurfaces and (b) shear bands.

491
492
493
494
495
496
497
498
499
500
501
502
503
504
505
506
507
508
509
510
511
512
513
514
515
516
517
518
519
520
521
522
523
524
525
526
527
528
529
530
531
532

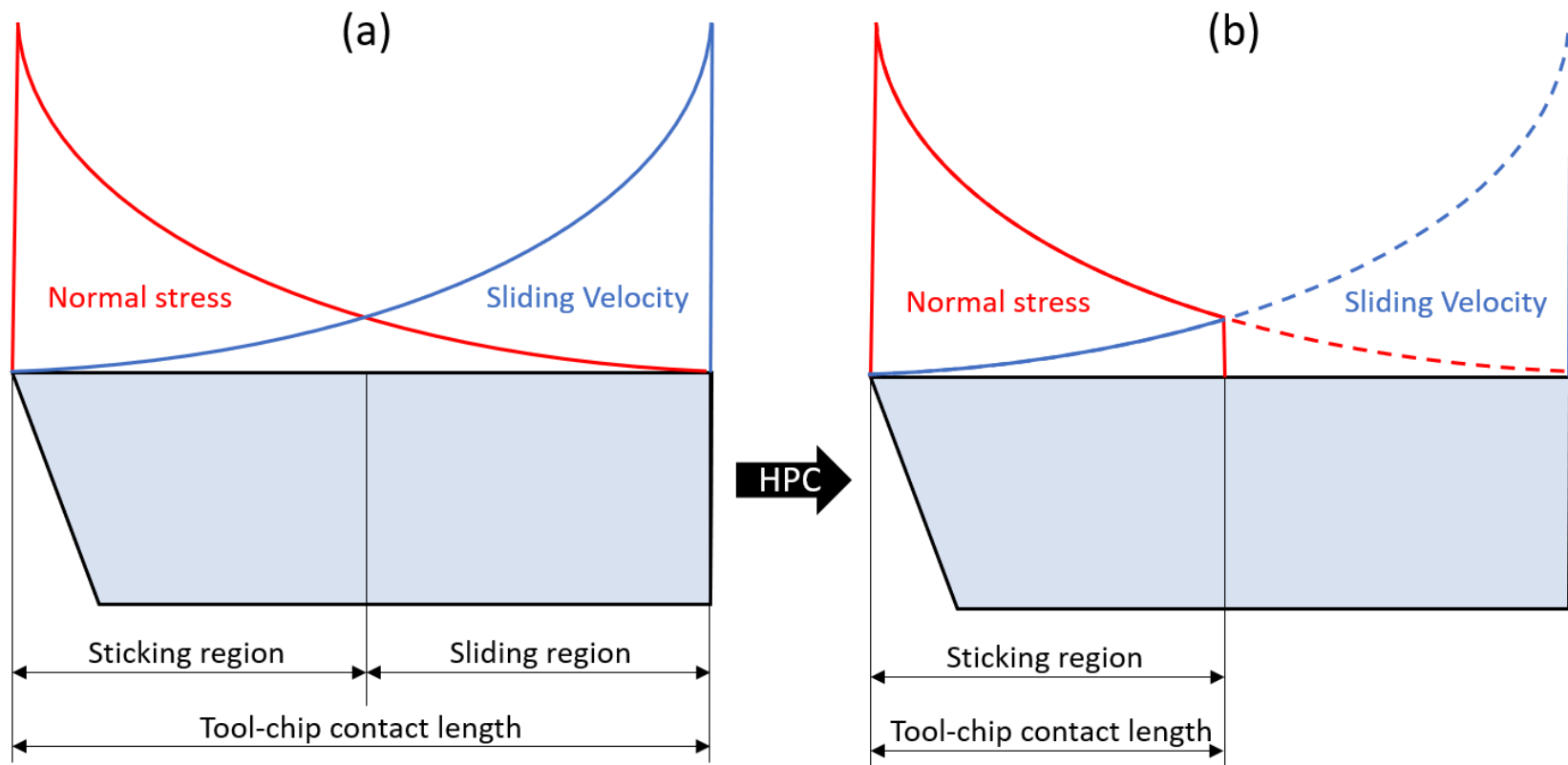


Fig. 12. – Tribological conditions along the rake face of the insert for (a) dry / flood, and (b) high-pressure coolant conditions.

533
534
535
536
537
538
539
540
541
542
543
544
545
546
547
548
549
550
551
552
553
554
555
556
557
558
559
560
561
562
563
564
565
566
567
568
569
570
571
572
573
574

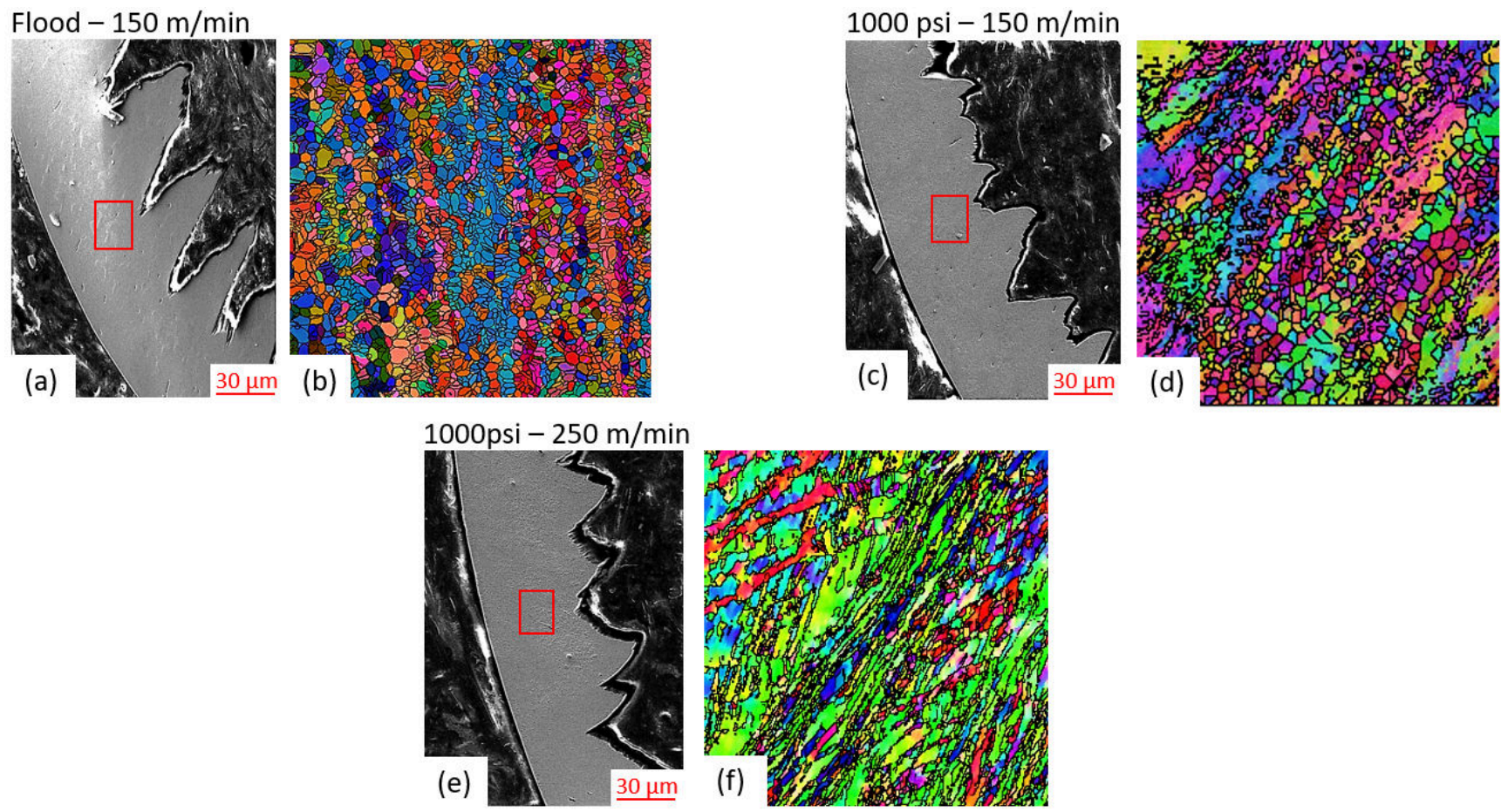


Fig. 13. – Chips cross-sections and EBSD orientation maps for (a,b) flood – 150 m/min, (c,d) 1000 psi – 150 m/min and (e,f) 1000 psi – 250 m/min.

575
576
577
578
579
580
581
582
583
584
585
586
587
588
589
590
591
592
593
594
595
596
597
598
599
600
601
602
603
604
605
606
607
608
609
610
611
612
613
614
615
616
617
618
619
620
621
622
623
624
625
626
627
628
629
630

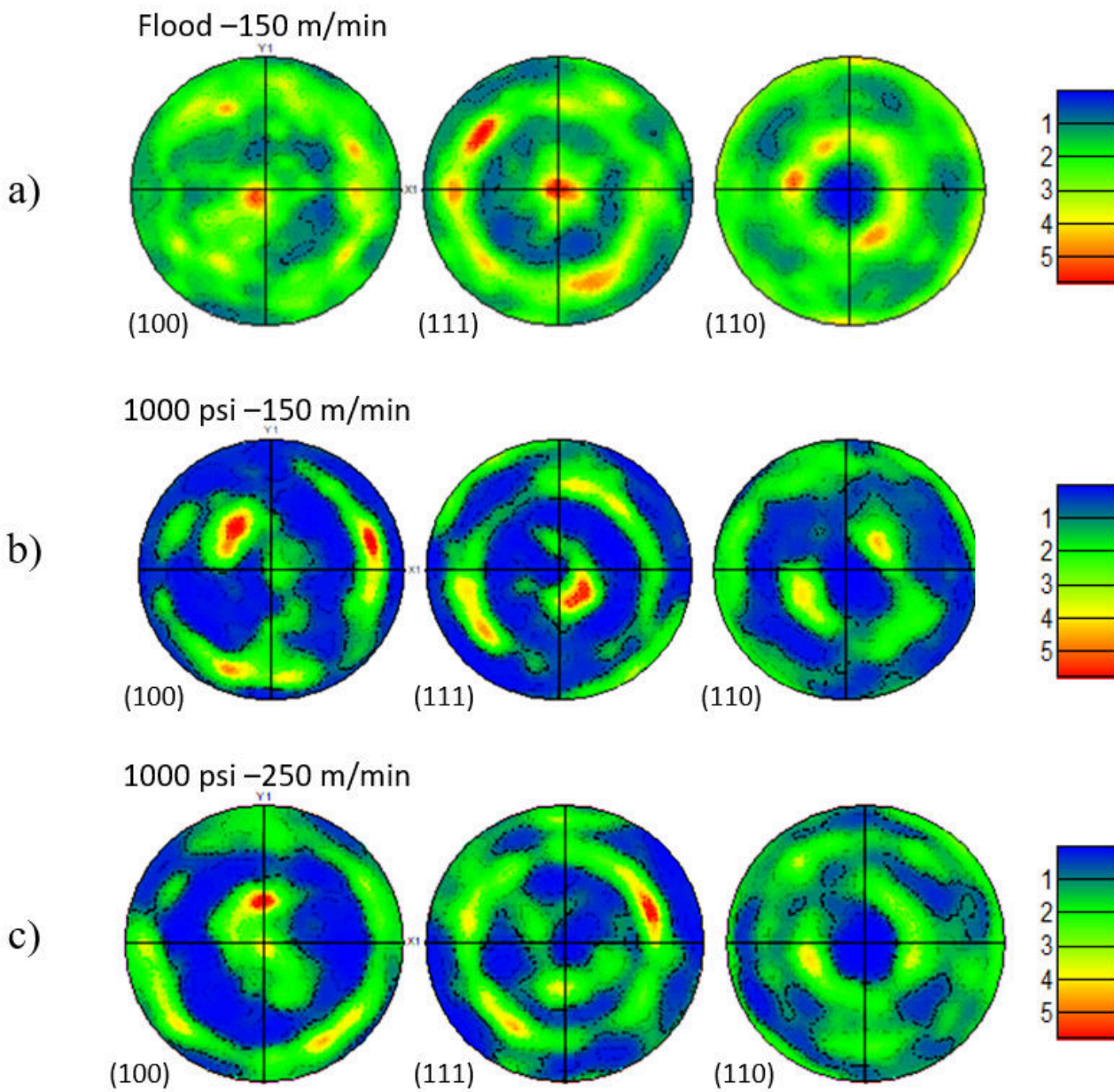



Fig. 14. – EBSD pole figures for (a) flood – 150 m/min, (b) 1000 psi – 150 m/min and (c) 1000 psi – 250 m/min.

Table 1. Simulation parameters for all the tested conditions.

Minimum element size (mm)	0.02
Maximum element size	0.1
Maximum number of nodes	24000
No. of output frames	30
Initial room temperature (°C)	20
Coolant heat transfer coefficient (W/m²K)	1x10 ⁴

1
2
3
4
5
6
7
8
9
10
11
12
13
14
15
16
17
18
19
20
21
22
23
24
25
26
27
28
29
30
31
32
33
34
35
36
37
38
39
40
41
42
43
44
45
46
47
48
49
50
51
52
53
54
55
56

Table 2. Chemical Composition, and main mechanical properties of Ti-6Al-4V at room temperature.

Element	Weight, max %	Yield Strength (MPa)	Tensile Strength (MPa)	Elongation %	Hardness (HB)	Thermal conductivity (W/m·°C)	T_{melt} (°C)
Al	5.5 – 6.75	828	895	10	341	6.6	1630
V	3.5 – 4.5						
N	0.05						
C	0.08						
H	0.015						
Fe	0.4						
O	0.2						
Residuals, each/total	<0.1 / < 0.4						

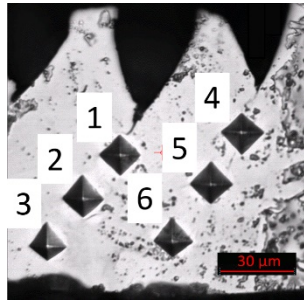
57
58
59
60
61
62
63
64
65
66
67
68
69
70
71
72
73
74
75
76
77
78
79
80
81
82
83
84
85
86
87
88
89
90
91
92
93
94
95
96
97
98

99
100
101
102
103
104
105
106
107
108
109
110
111
112
113
114
115
116
117
118
119
120
121
122
123
124
125
126
127
128
129
130
131
132
133
134
135
136
137
138
139
140

Table 3. Machining parameters for experimental testing.

	Coolant pressure (psi)				Feed (mm/rev.)	DOC (mm)
	Flood (Benchmark)	400	800	1000		
Vc (m/min)	150				0.1225	0.25
	n/a	200				
	n/a	250				

Table 4. Shear band chips microhardness profiles for flood – 150 m/min, 1000 psi – 150 m/min and 1000 psi – 250 m/min with values highlighted for the points located near the tool-chip interface.



	Hardness (HV)					
	1	2	3	4	5	6
Flood – 150 m/min	337	365	361	306	330	354
1000 psi – 150 m/min	354	365	392	354	396	380
1000 psi – 250 m/min	373	363	434	343	338	408

Tool-chip interface

Tool-chip interface

141
142
143
144
145
146
147
148
149
150
151
152
153
154
155
156
157
158
159
160
161
162
163
164
165
166
167
168
169
170
171
172
173
174
175
176
177
178
179
180
181
182

1
2
3 **Research highlights**
4
5
6

- 7 • Oxidation wear is reduced by the application of HPC.
- 8
- 9 • An increase in the heat generation by plastic deformation for the HPC condition.
- 10 • Coolant pressure and maximum flank wear are inversely proportional to each other.
- 11
- 12 • The chip formation process is facilitated by the application of HPC.
- 13
- 14 • Chips are strain hardened with the application of HPC.
- 15
- 16
- 17
- 18
- 19
- 20
- 21
- 22
- 23
- 24
- 25
- 26
- 27
- 28
- 29
- 30
- 31
- 32
- 33
- 34
- 35
- 36
- 37
- 38
- 39
- 40
- 41
- 42
- 43
- 44
- 45
- 46
- 47
- 48
- 49
- 50
- 51
- 52
- 53
- 54
- 55
- 56